

Article

Dimensional Accuracy of Electron Beam Powder Bed Fusion with Ti-6Al-4V

Eric Bol and Mamidala Ramulu * 

Mechanical Engineering Department, College of Engineering, University of Washington, Seattle, WA 98195, USA
* Correspondence: ramulum@uw.edu

Abstract: While much of additive manufacturing (AM) research is focused on microstructure, material properties, and defects, there is much less research in regards to understanding how well the part coming out of the machine matches the 3D model it is based on, as well as what are the key process parameters an engineer needs to care about when they are optimizing for AM. The purpose of this study was to understand the dimensional accuracy of the electron beam powder bed fusion (EB-PBF) process using specimens of different length scales from Ti-6Al-4V. Metrology of the specimens produced was performed using fringe projection, or laser scanning, to characterize the as-built geometry. At the meso-scale, specimen geometry and hatching history play a critical role in dimensional deviation. The effect of hatching history was further witnessed at the macro-scale while also demonstrating the effects of thermal expansion in EB-PBF. These results make the case for further process optimization in terms of dimensional accuracy in order to reduce post-processing costs and flow time.

Keywords: electron beam; powder bed fusion; dimensional accuracy; titanium



Citation: Bol, E.; Ramulu, M. Dimensional Accuracy of Electron Beam Powder Bed Fusion with Ti-6Al-4V. *Designs* **2023**, *7*, 53. <https://doi.org/10.3390/designs7020053>

Academic Editor: Obeidi Muhannad

Received: 28 February 2023

Revised: 31 March 2023

Accepted: 31 March 2023

Published: 6 April 2023



Copyright: © 2023 by the authors. Licensee MDPI, Basel, Switzerland. This article is an open access article distributed under the terms and conditions of the Creative Commons Attribution (CC BY) license (<https://creativecommons.org/licenses/by/4.0/>).

1. Introduction

Titanium alloy Ti6AL4V is the workhorse of the aerospace and medical industries due to its strength, density, durability, and corrosion resistance. These industries place a high priority on product safety, so dimensional accuracy must be well understood and high-quality manufacturing repeatability must be proven. When Ti-6Al-4V is converted into a powder through atomization processes and used as an additive manufacturing feedstock for electron beam powder bed fusion (EB-PBF) or laser beam powder bed fusion (LB-PBF), fully dense titanium hardware can be produced. This method of AM uses an electron beam as the energy source to selectively melt powder that is uniformly distributed within a build chamber in a layer-by-layer process. With this technology, increasingly complex structures can be designed and manufactured that could not be cost-effectively produced any other way [1].

In-situ process monitoring of the EB-PBF process is extremely difficult because the build chamber environment is a vacuum and heated to high temperatures, approximately half of the material melt temperature (~650 °C for titanium) [2–5]. In addition, the electron beam scan speed is very fast and is typically split into many points to maintain simultaneous melt pools [6]. Thus, it remains challenging and an active area of research to identify the nuances of what is happening with the beam power and the interaction with the melt pool. Key features of as-built EB-PBF specimens are often the surface morphology, or surface roughness, and their microstructure. Typically, EB-PBF uses a larger powder size distribution (PSD) than laser PBF machines, ranging from 45 to 106 µm in diameter, and it is one of the primary contributing factors to surface roughness [7]. The larger particles are used because they are more resistant to “smoking”, or powder spreading, which is the buildup of excessive negative charge energy that forces the displacement of particles in all directions from the powder bed [8]. Process parameters, such as the beam speed, beam

current, beam focus, scan strategy, etc., can have a significant effect on the resulting surface roughness, such that optimization can provide improvements to dimensional accuracy [9].

The as-built surface roughness of electron beam and laser PBF parts has been well documented, with numerous methods of metrology being implemented in attempts to characterize it [10–20]. Most focus on the surface-connected pores and partially melted attached particles that are difficult to describe by areal texture parameters defined in ISO 25178-2. The surface roughness of the top layer during the build has not been looked at in detail as it is subsequently remelted by the following layer. However, the recently melted topography affects how that next layer of particles is distributed, as well as the overall dimensional variation.

For traditional manufacturing, geometric dimensioning and tolerance (GD&T) standards have been well established based on ISO, ASME, and ASTM standards. The highly optimized and complex 3D structures that PBF can produce pose a challenge for traditional inspection and quality assurance methods. In the early stages of AM development, not much distinction was made between accuracy and resolution, particularly for prototype fabrication; however, with the expectation that AM will deliver high-quality finished production parts, there is a need for new or modified methods of measuring dimensional accuracy [21–23]. Various methods of optical 3D scanning are typically used to generate point clouds and then fit surfaces to the data to be compared with the CAD model.

Smith et al. used 3D scanning of optimized truss structures to measure dimensional deviation, yet found it difficult to determine if the variation seen in the measurements was true or if the specimens had been deformed when being manipulated for scanning [24]. In a study performed by Ameta et al., the authors introduced the concept of derived supplemental surfaces (DSS) based on "theoretical supplemental surfaces" (TSS) in ASME Y14.46 [25]. They measured a lattice structure using a laser confocal microscope, which generated a point cloud, and fitted the DSS using the Chebyshev and least-squares approaches. Gruber et al. used a fringe projection 3D scanning system and CT scans to analyze benchmark samples for geometric accuracy, and they found both were well suited for determining external feature part quality [26]. However, while most studies have focused on the accuracy of the particular metrological method employed, few have used multiple methods in tandem to characterize the dimensional accuracy of an AM process.

Previous work that revealed the dimensional deviation of a single beam width line melt and the optimization of an assembled structure were presented to ASME [27,28]. The purpose of this paper was to quantify the dimensional accuracy at different length scales in the EB-PBF process and identify sources of deviation for further improvement. Two experiments were conducted using Ti-6Al-4V powder, where the meso-scale experiment produced step and ramp specimens that measured variation based on layer topography, thickness, and build location, and the macro-scale experiment produced tapered box beams that had been topology optimized and used a 3D laser scanner to measure the as-built geometric dimensional deviation. These experiments demonstrated how important process optimization is for controlling variation from the initial layers to the final component quality.

2. Materials and Methods

2.1. EB-PBF Process

For the experiments described in this work, all samples were manufactured utilizing reused gas-atomized Grade 5 Ti-6Al-4V powder, originally obtained from the EB-PBF machine manufacturer, with a powder size distribution (PSD) of 45–106 μm in diameter. The EB-PBF process was performed with an Arcam A2X, shown in Figure 1, utilizing the default parameters provided by the machine manufacturer for Ti-6Al-4V that are organized into themes. The A2X emits electrons from an electrically heated tungsten filament with 60 keV of power acceleration and a current range from 0 to 50 mA. Because electrons will interact with atoms in the atmosphere, the process must take place within a high vacuum (normally 1×10^{-5} mbar) environment; however, a small amount of helium pressure is applied (2×10^{-3} mbar) to avoid oxygen contamination as well as reduce the amount

of electrostatic charge buildup in the powder material. Three electromagnetic lenses that affect the spot shape, size (typically 250 μm in diameter), and position guide the beam to the powder bed. The method of energy transfer from the electrons to the powder bed material is by way of kinetic energy with elastic and inelastic collisions. In order to further reduce the risk of powder overcharge resulting in “smoking,” an unfocused beam is employed to preheat the start plate and the powder bed prior to using a focused beam for melting [2,8,29,30].

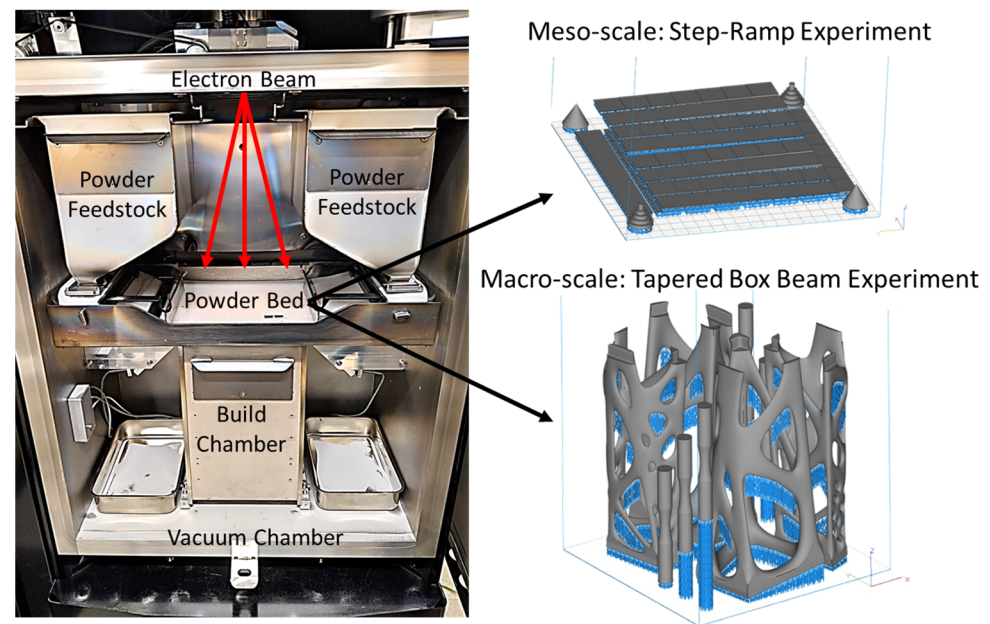


Figure 1. Image of the Arcam A2X EB-PBF experimental setup along with the build volume input models of the meso-scale step-ramp experiment and the macro-scale tapered box beam experiment. The experimental specimens are colored gray, while support features are shown in blue.

Process parameters for the experiments were grouped into four themes defined as start plate preheat, powder layer preheat, melt, and wafer (for support features). During the machine setup, the start plate preheat and powder layer preheat themes are set for the entire build, while the melt or wafer themes are assigned to individual parts, including supports. For example, the wafer theme parameters create a lower energy-dense beam to reduce the melt consolidation between layers, so that support features would be easier to remove in post-processing. A layer thickness of 50 μm was specified for all experiments, and a 210 mm \times 210 mm \times 10 mm SS316L start plate was utilized.

The printing process began with the start plate preheating to 730 $^{\circ}\text{C}$, as measured by a thermocouple located directly beneath the start plate. Once the target temperature was reached, a layer of powder was fetched from the hoppers and distributed evenly across the build area by a rake. Every new layer proceeds with a preheat conducted in two stages defined by the Powder Layer Preheat theme. Preheat 1 scans the entire powder bed to bring the powder temperature to a “jump-safe” level, and then preheat 2 rescans the powder where melting is to occur, plus an offset, to further raise the powder temperature to a “melt-safe” level. Preheat 1 and 2 sinter the powder bed to prevent the powder from spreading when it is impacted by a focused beam for melting.

Following the preheat phase, the specimen outlines were melted using the contouring parameters and a spot-melt scan strategy. That was followed by an infill hatching scan, which rastered the beam back and forth. While contours are performed at a constant beam power, the hatching scan is continuously varied by four proprietary functions designed to keep the melt pool properties consistent. The current compensation function sets the beam current based on the length of the hatch line, while the speed function varies the velocity based on the beam current for a consistent melt pool size. The turning point function

reduces the beam energy near the beginning of each hatch line, and the thickness function reduces the beam energy when melting close to an overhanging surface [24]. All of these parameters reside within the definition of the melt theme.

2.2. Experimental Design

Some level of distortion in welding and metal PBF is expected, and melting thin sheet metal was anticipated to amplify the dimension deviation. Therefore, for the meso-scale experiment, thin step and ramp specimens were designed as shown in Figure 2. The thinnest specimens started at 0.1 mm (2 layers) and gradually increased in thickness to 0.7 mm (14 layers), while the thicker specimens began at 0.2 mm (4 layers) and increased to 1.4 mm (28 layers). Each specimen was 140 mm long and 20 mm wide. Along the length, step specimens were divided into 7 steps of constant thickness, increasing at either 0.1 mm or 0.2 mm increments, while ramp specimens continuously increased from the starting thickness until reaching the final thickness and maintaining that constant for the final 20 mm. For the step specimens, the thickness-to-length ratio ranged from 0.5% to 3.5% and 1% to 7% for the thin and thick designs, respectively. Ramp specimens were designed to have a slope of 0.005 ($\theta \approx 0.29^\circ$) and 0.01 ($\theta \approx 0.57^\circ$) for the thin and thick designs, respectively. At these angles, the stair-case effect of the layering process will reveal the melt topology at every layer.

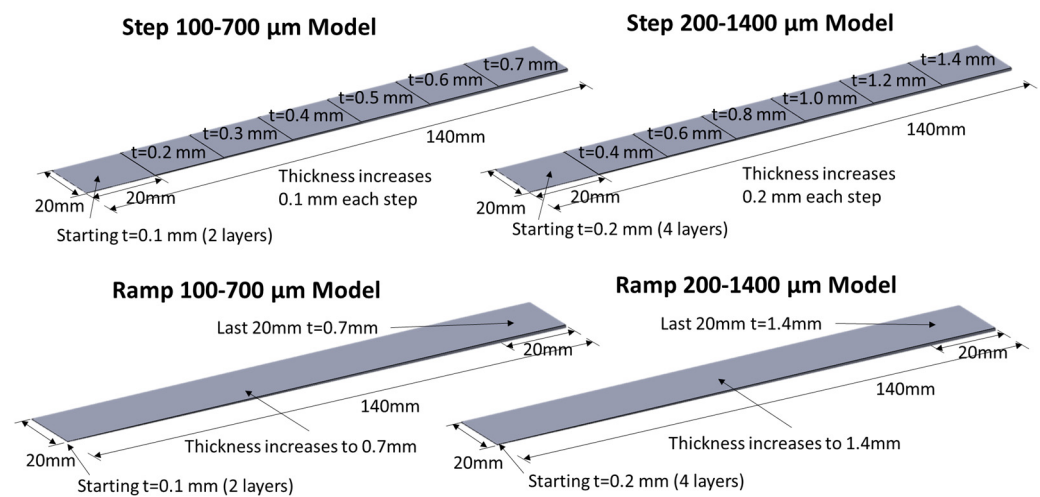


Figure 2. Meso-scale experiment specimen design illustrating the dimensions of the thin and thick CAD models of step and ramp.

The build for this experiment manufactured four sets of the four specimens from Figure 2, and the build volume configuration is presented in Figure 3. The first set of four specimens were lined up, side by side, 5 mm above the start plate, with skin surface supports extending to the plate. That same model setup was repeated adjacently but started at 7 mm above the start plate with supports extending to the start plate. Then that pattern of eight specimens was repeated at a higher location in the build volume, starting at 18.4 mm, oriented perpendicular to the previous set. Each upper specimen was provided with supports matching the first set, extending 5 mm below into the sintered powder but not extending to any other structures or the start plate. The lower (L) specimens were numbered L1 through L8, while the upper (U) specimens were numbered U1 through U8. The odd numbers are ramp models, while the even numbers are step models.

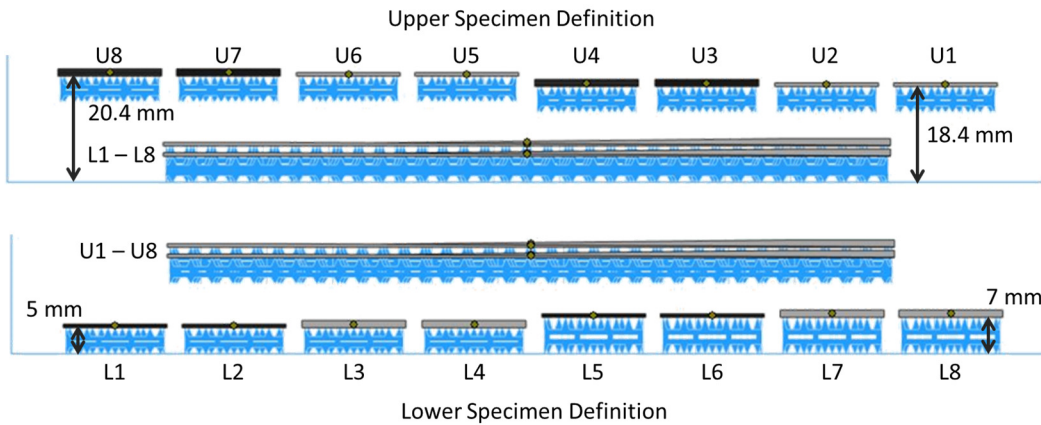


Figure 3. Meso-scale experimental design showing the side views of the build volume with specimen labels and build height dimensions of the upper and lower specimen sets. The experimental specimens are colored gray, while support features are shown in blue.

For the macro-scale dimensional accuracy experiment, a topology-optimized tapered box beam was selected as the specimen. The box beam design is based on the forward strut box of a fan case-mounted turbofan engine pylon and scaled down to a size just slightly larger than the Arcam A2X volume, such that it was necessary to be split into halves and assembled. Commercially available topology optimization software that contains a proprietary implementation of the SIMP (solid isotropic material with penalty) method [31–34] was employed as a guide for where to place material using mass-minimization criteria. The result guided follow-on design refinements based on maximum principal stress minimization criteria under bending and torsional loads. Further redesign efforts focused on elements of Design for Additive Manufacturing (DfAM) criteria such as build orientation, support minimization, powder removal, and method of assembly. The final design of the topology-optimized tapered box beam is displayed in Figure 4.

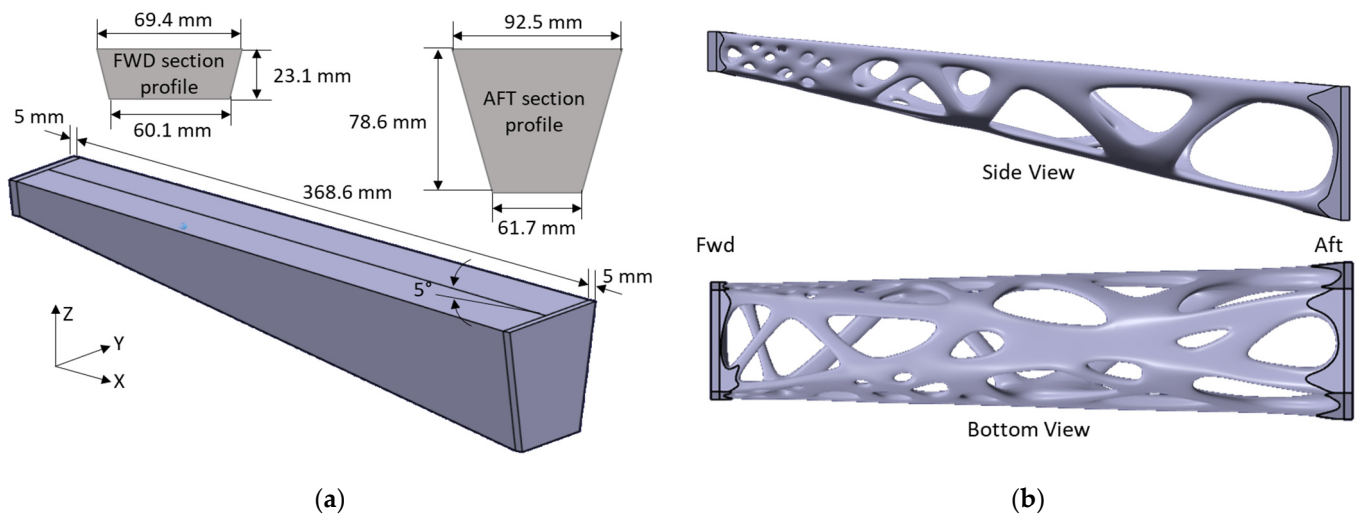


Figure 4. Macro-scale dimensional accuracy specimen design illustrating the: (a) design space dimensions; and (b) the final overall shape of the tapered box beam design showing the side view and bottom view.

Six beam specimens were produced over three builds, two per build, as shown in Figure 5. The beams are labeled with the nomenclature “Front” (F) and “Back” to distinguish their location within the build chamber, with the front being closest to the build chamber door. By placing the mid-span joint furthest from the build plate in the z-direction, the goal was to magnify any dimensional deviation present in the buildup of the layer-by-

layer process. The interfacing surfaces at the three joint locations were designed such that the two halves would slide together axially with a surface clearance of 0.1 mm. This was done to create a tight fit based on the mechanical-chemical bonding strategy, where the interfacing surfaces were solution cleaned with acetone, sanded with a diamond rotary tool, then solution cleaned again, before being bonded using JB Weld and curing while clamped for >24 h.

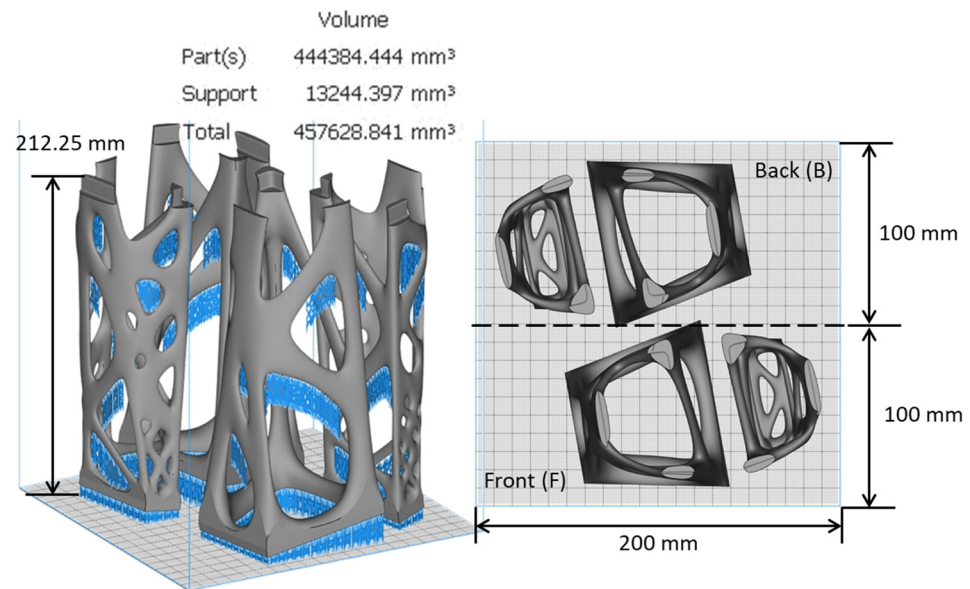


Figure 5. Macro-scale tapered box beam experiment: build support strategy and build volume layout identifying the front and back specimen locations. The experimental specimens are colored gray, while support features are shown in blue.

2.3. Metrology

The topology of the step and ramp specimens was measured using a Keyence VR-3100 three-dimensional profile measurement microscope, which utilizes high-intensity LED light and a 4-megapixel monochrome CMOS to obtain a one-shot fringe projection image. Fringe projection enables the instantaneous measurement of the length, height, volume, angle, etc. of a portion of any object. Prior to examination, the specimens were post-processed using the Arcam Powder Recovery System (PRS). Due to the differing materials between the steel start plate and the titanium specimens, during cooling the interfacing welds cracked such that the specimens were removed by hand without cutting. The down-skin support features were not removed in order to provide a more stable orientation on the imaging platform, and for each specimen, several images were taken at 40× magnification and stitched together using the system software in order to capture the entire length.

The geometric accuracy of the assembled topology-optimized tapered box beams was determined by a 3D laser scan. A Kreon Ace measuring arm, mounted to a calibrated table, was combined with a Skyline 3D scanner that specifies an accuracy of up to 9 μm. Each specimen was placed on the table in various orientations while the operator manually manipulated the scanner by hand, sweeping along the surface of the part without contact in multiple passes. The scanner utilizes an HD camera and blue laser so that it can measure reflective materials like titanium, and it generates a dense point cloud to capture the surface topology with a scan speed of up to 600,000 points per second. Software assembled the point clouds into a single topological surface per beam and then converted them to an STL file. Metrology analysis was accomplished using GOM Inspect software, which examined the parameters of total length and total volume based on an overall best fit compared to the nominal CAD geometry.

3. Results

In this section, the results of the multi-scale manufacturing experiments and metrological analysis of the step-ramp and tapered box beam specimens are presented. In addition, witness coupons were also produced to examine the microstructure and tensile properties of the additively produced samples. These aspects and others are important to consider for any sort of part or process qualification and are briefly reported in Figure 6. From the SEM image of the microstructure taken from specimen L2, the dual phase of fine lamellar α and β that appears as a basket weave (Widmanstätten) is expected from Grade 5 Ti-6Al-4V [35]. The tensile properties reflect a more brittle Ti-6Al-4V, which can be expected from heavily reused powder feedstock, with only about 4% elongation but very high yield strength (0.2% offset) of 1097 MPa and an elastic modulus of 103 GPa.

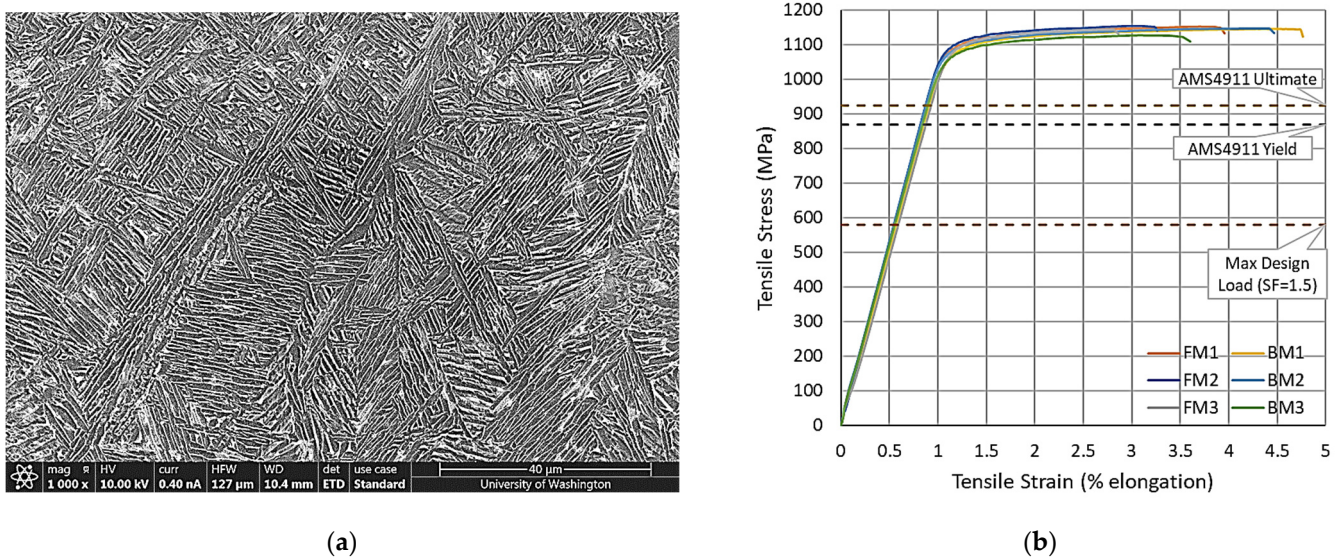


Figure 6. Properties of the additively produced specimens: (a) SEM image of specimen L2 microstructure at the 500 μm design thickness (up is the build direction); and (b) tensile properties taken from tapered box beam specimen builds 1–3, while also displaying comparisons for AMS 4911 and the maximum design load criteria.

3.1. Meso-Scale Step-Ramp Experiment

The top surfaces of the fringe projection images of step and ramp specimens, L1 through L4, are displayed in Figure 7, with the designed thickness of the layers identified. From the ramp specimens, L1 and L3, the staircase effect of the layering process is clearly shown, which also provides the hatching pattern and angle that occurred on every layer. step specimens L2 and L4 provide a good contrast with large 20 mm \times 20 mm melt areas. On the left-hand side of the specimens L1 and L2, the thinnest 100 μm thickness (two layers) shows an enormous quantity of pores, many of which contain partially melted or sintered powder inside. The thinnest layers of L3 and L4 have only a few pores because they started at four layers thick and can be directly compared with the 200 μm levels in L1 and L2. Progressing upward in designed thickness, random pores were still present in various specimens and layers. Typically, these pores were found at the intersection of the contour and hatch scans, or at what appeared to be the stop or start of a hatch scan.

As observed due to the variation in contrast, there was a lack of uniformity in the hatching melt at every layer on every specimen. Some hatch lines appeared wide and well melted, while in some cases, a few millimeters away, the lines are thin and raised such that they appear to not be touching the adjacent lines. Several hatch lines also appear to meander along the scan direction. These optical differences are more clearly visualized in three dimensions, as shown in Figure 8, using an example from L3 at the 550 μm design thickness. Optically, the shading reveals that very few layers appear to have a completely

uniform melt despite a constant thermal mass. The 450 μm layer of L1 and L3 appears to have the most uniform melt, whereas on other layers there exists a significant contrast in the hatch scan melt, particularly in the ramp specimens L1 and L3.

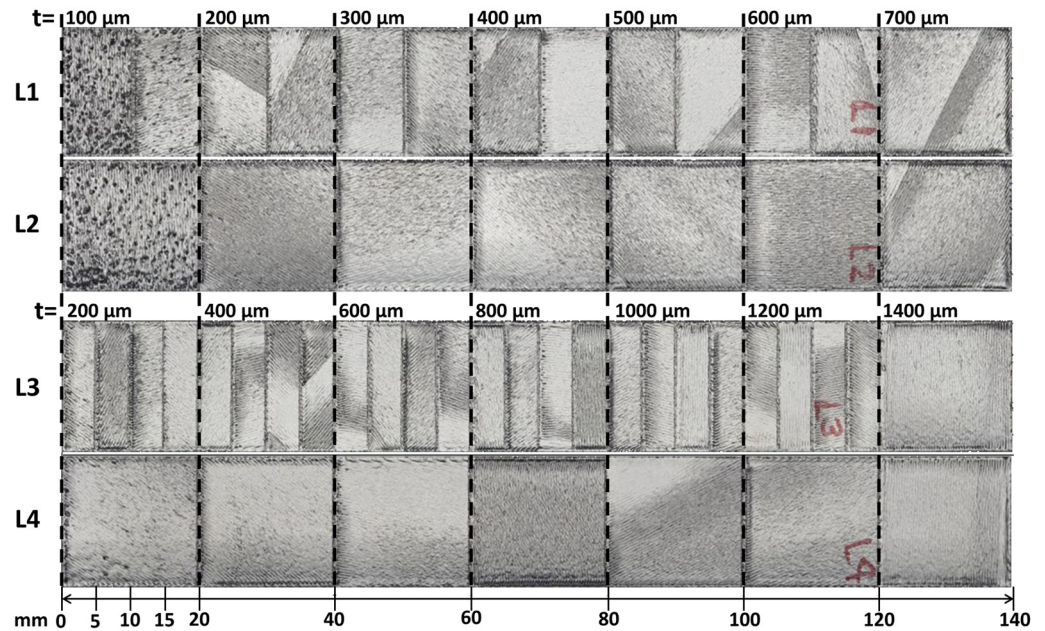


Figure 7. Set 1 of 4 step and ramp specimens, L1 through L4, from top to bottom, with the designed thickness indicated in black text starting at the dashed lines.

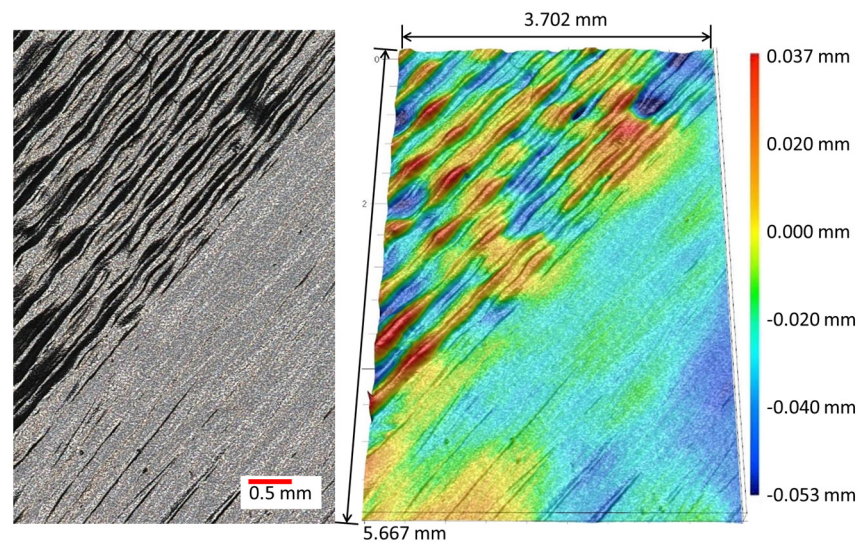
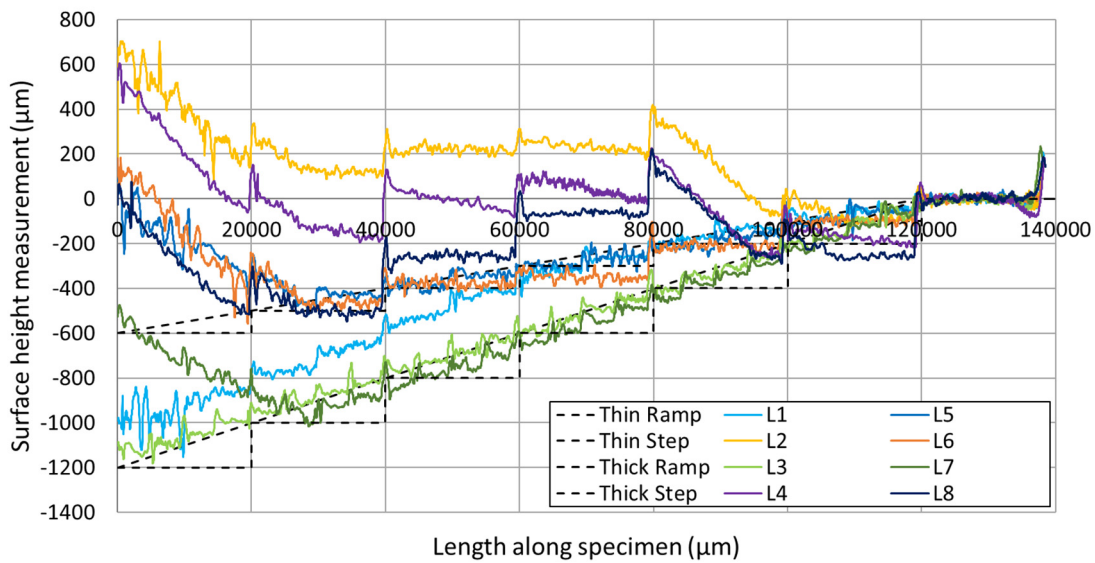
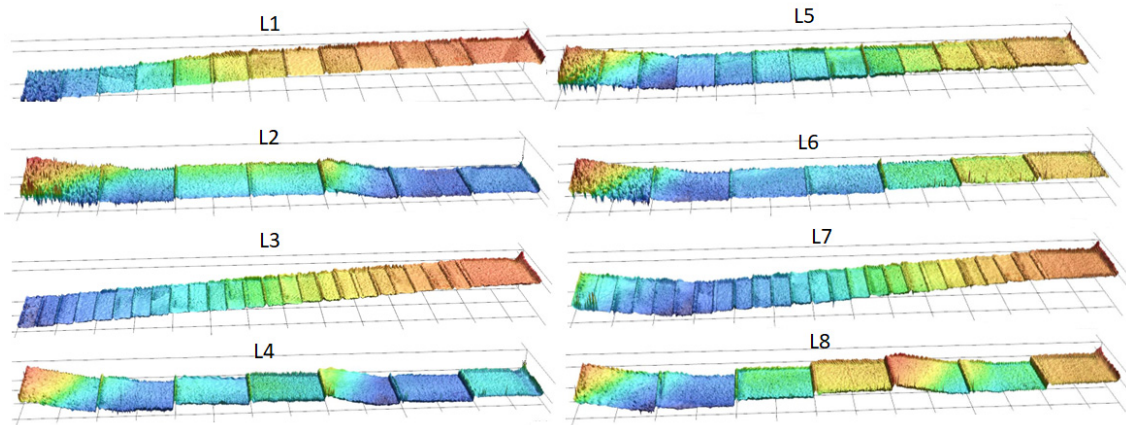


Figure 8. Specimen L3, Layer 8 (550 μm design thickness), 40 \times optical image (left), and 3D height data image (right). This image displays a transition in the scan lines melt quality and surface roughness within a single layer.

Height data was analyzed to extract a topological centerline profile of the specimens along their length. This is shown in Figure 9 compared to the CAD file dimensions to demonstrate the level of dimensional accuracy in the thin and thick specimens. As there were no perfectly flat regions with which to calibrate a zero plane, the top layer, being the most consistent, established the zero-reference plane for specimens L1 through L8. The contour scan created raised ridges around the periphery of each layer, and these are depicted as sharp spikes in the plot, occurring at regular 5 mm, 10 mm, or 20 mm intervals depending on the specimen geometry.



(a)



(b)

Figure 9. Upper surface measurements of the lower thin and thick ramp and step specimens: (a) centerline profile versus the expected CAD geometry; (b) three-dimensional surface height plots provided as graphical representations of specimens L1 through L8, where the desired behavior is to gradually transition from blue to red as demonstrated by L3 (colors are not set to the same scale).

As anticipated, these thin titanium specimens were distorted from their CAD geometry. The only exception was the thicker ramp specimen, L3, which most closely matched the CAD profile, only deviating by about 50 µm in the thinnest 200 µm region. Specimens L5, L6, and L7 also showed good agreement with the CAD profile beyond the thinnest 30 mm of the span length, but prior to that point, veered sharply upwards by a total of 600–700 µm. Specimen L1 still resembles a ramp, but distorts downward a total of 300 µm, from the mid-span to the thinner regions, at a rate of 10 µm in height per mm.

Other than L6, the step specimens (L2, L4, and L8) all displayed a different mode of distortion from the ramp specimens, indicating the level of dimensional accuracy in EB-PBF is affected by the geometry being manufactured. Relative to the top step surface, the thin and thick step specimens deviated sharply upwards at the 5th step, and only a few steps appear flat. Most of the steps appear to have a different slope, and the total deviation for L2, L4, and L8 was approximately 1.25 mm, 1.8 mm, and 1.3 mm, respectively, along the 140 mm length.

The remaining upper specimens U1–U8, that were manufactured off of the build plate with floating supports, showed significantly higher levels of dimensional deviation,

particularly at the extremities, ranging from 2 mm to 4 mm. Those eight specimens were distorted to the point that an adequate reference plane could not be established from which to make direct comparisons. However, the middle thickness regions of the upper specimens agreed with the CAD geometry, similar to what L3 and L7 demonstrated. Overall, dimensional accuracy is typically worse when associated with large flat surfaces that are parallel to the build plane. No two specimens of the same CAD geometry demonstrated the same distortion behavior.

Shading differences in the upper surface topography in Figure 7 clearly show differences in hatching scan angles for different layers. It is well known that AM machines will rotate the hatching angle between layers as a method to reduce anisotropy in the material microstructures and prevent large grain growth in the build direction. Because the ramp specimens revealed the hatch topography for every layer, a closer inspection of the hatch angles was performed with the expectation that the hatching angle would be the same within any given layer across all specimens. Figure 10 plots the exposed hatch angles for each specimen for the given design thickness layers.

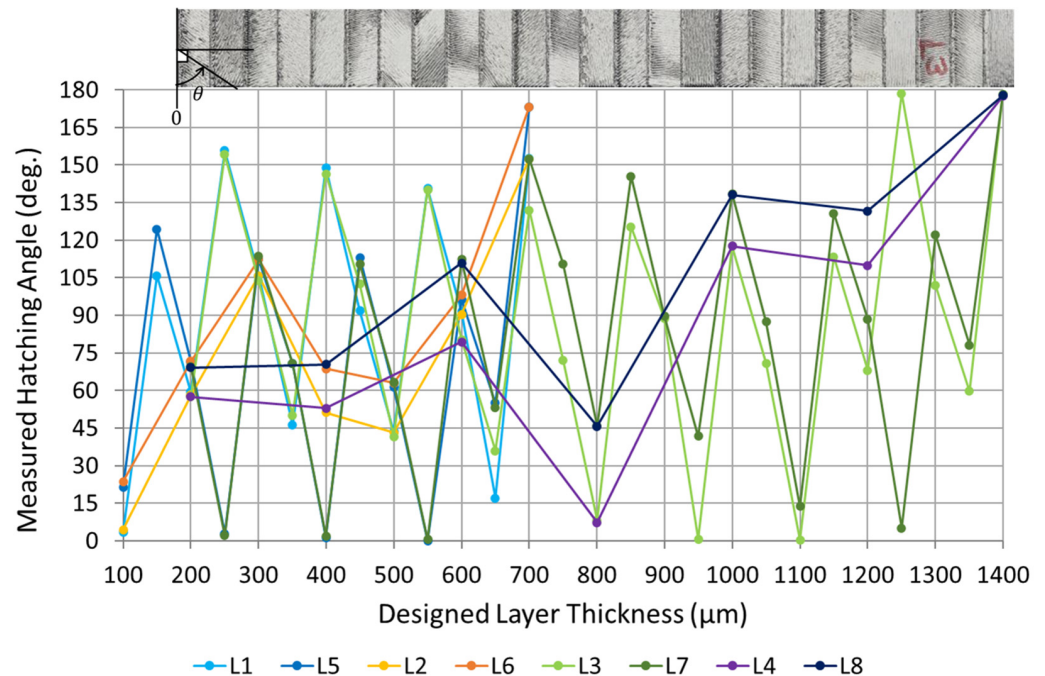


Figure 10. Hatching scan angles for specimens L1-L8 as measured by visual inspection of the optimal images.

For example, at the 200 µm level, specimens L1-L4 are all hatched with a 58-degree scan angle, while L5-8 were hatched with a 70-degree scan angle. However, at 400 µm, L1 and L3 were hatched at a 147-degree scan angle, while the immediately adjacent specimens L2 and L4 were hatched at a 52-degree angle. While a few degree measurement error may exist in the accuracy of the visual inspections, it cannot account for a 95 degree difference. At that particular layer, the machine software chose to melt the ramp specimens, which were not next to each other, at a vastly different angle than the step specimens. Figure 10 reveals that no two specimens, regardless of the geometry or build location, have the same hatching angle history, which would explain the variations in dimensional accuracy.

3.2. Macro-Scale Beam Experiment

Following fabrication, the topology-optimized tapered box beam specimens exhibited a rough as-built surface condition that is typical of the powder bed fusion process. Surface curvature and space-frame member transitions of the parts in this experiment were smooth, without facets, and surfaces opposite the build direction that were not supported had a

rougher surface than parallel or top surfaces. Since the components were at an angle such that no final surface was parallel with the build plane, a fairly uniform surface condition was obtained. Support features were manually removed with dykes and smoothed using a tungsten carbide rotary tool, while both the forward and aft ends of the beam were ground flat with a belt sander. Figure 11 shows a fully bonded beam specimen as well as a portion of the 3D scan data showing surface features and missing surface regions. All six beams were successfully assembled, which demonstrated the geometric accuracy based on a CAD interface clearance of only 0.1 mm.

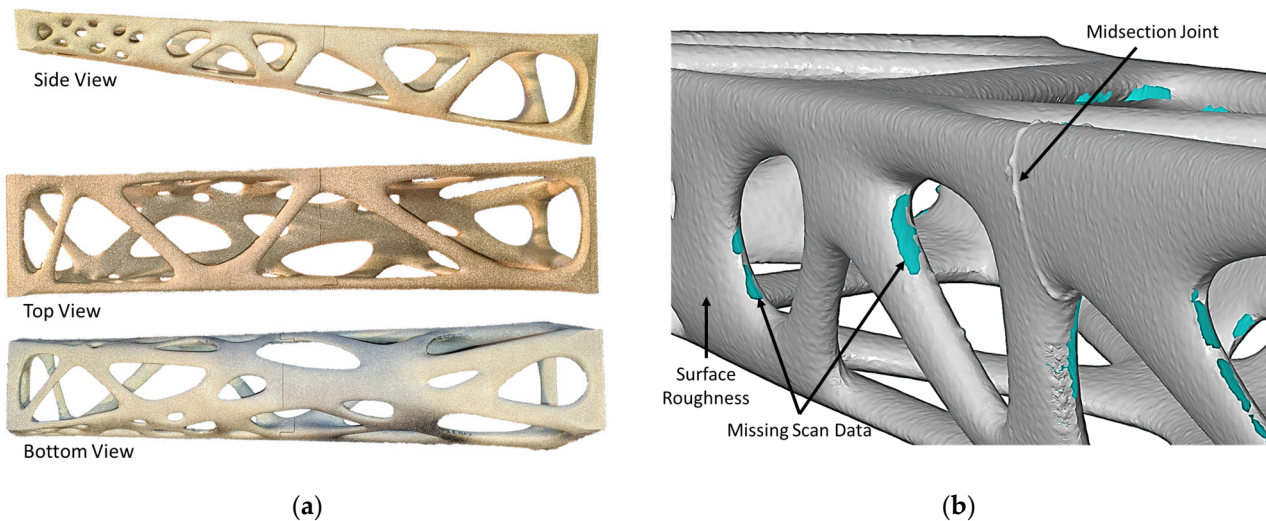


Figure 11. Macro-scale specimen of a topology-optimized taper box beam manufactured from Ti-6Al-4V via the EB-PBF process: (a) Side, top, and bottom view images, respectively, of one assembled specimen; (b) Example section of scanned STL data from specimen 1F.

A surface-best fit comparison of the six sets of scanned geometry to the CAD model had good results with alignment despite the absence of datum features. The alignment primarily matched the middle of the beams, such that the largest deviations in accuracy were revealed at the forward and aft extremities. Generally, all of the beam specimens were smaller than the CAD model. When overlaid with the nominal geometry, the outer surfaces of the scanned data were either equal to or inside the nominal surface, implying the printed beams had all thermally contracted as they cooled. The contraction is most notable at the forward and aft ends of the beams, as can be seen in the side views of Figure 12, where the transparent gray CAD surface protrudes beyond the colored scan surface. Scanned surfaces were only observed protruding from the CAD model on the inner surfaces of the beam that are depicted in yellow and red.

Figure 13 displays the results of the length and volume measurements of each of the six beam specimens. The designed nominal length (L_0) from the aft plane to the forward plane was 378.59 mm; however, the longest specimens, 3B (build: 3, location: back) and 1B (build: 1, location: back), were measured at 376.4 mm, 2.19 mm shorter than nominal. Specimen 3F (build: 3, location: front) was the shortest of the 6 beams, which measured 376.14 mm, 2.45 mm shorter than nominal. This provides a deviation range across the six beams of only 0.26 mm. The average length of the six beams was 376.29 mm, which is 2.30 mm, or 0.6%, shorter than nominal, but with a standard deviation of only 0.036%, or 0.10 mm (0.004 inches).

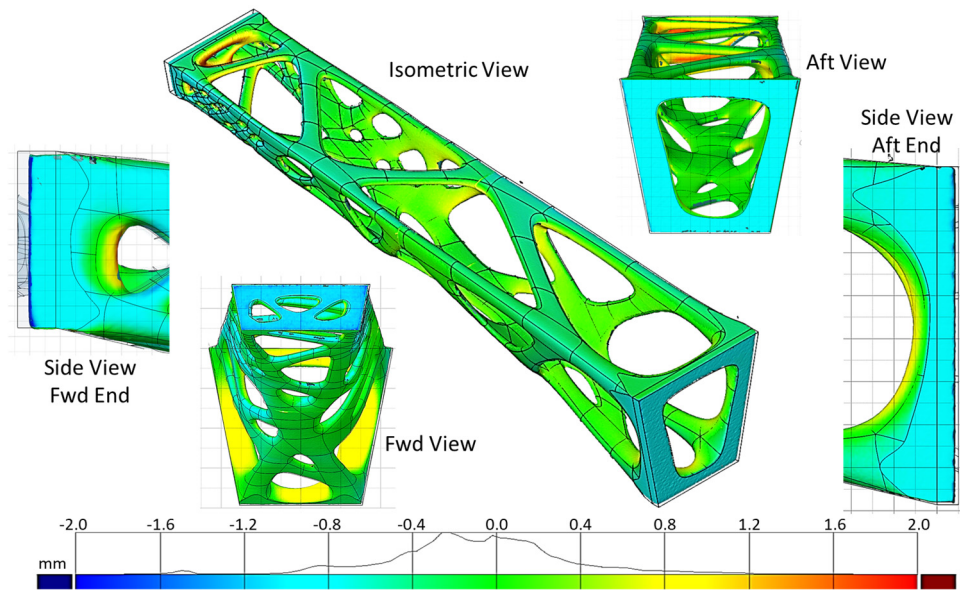


Figure 12. Example of geometric best-fit surface analysis comparison to nominal CAD using scan results of specimen 1F. The scanned surface is overlaid with a transparent CAD model, where blue indicates that the scanned surface resides inside the CAD geometry and yellow indicates that it is protruding from the CAD geometry.

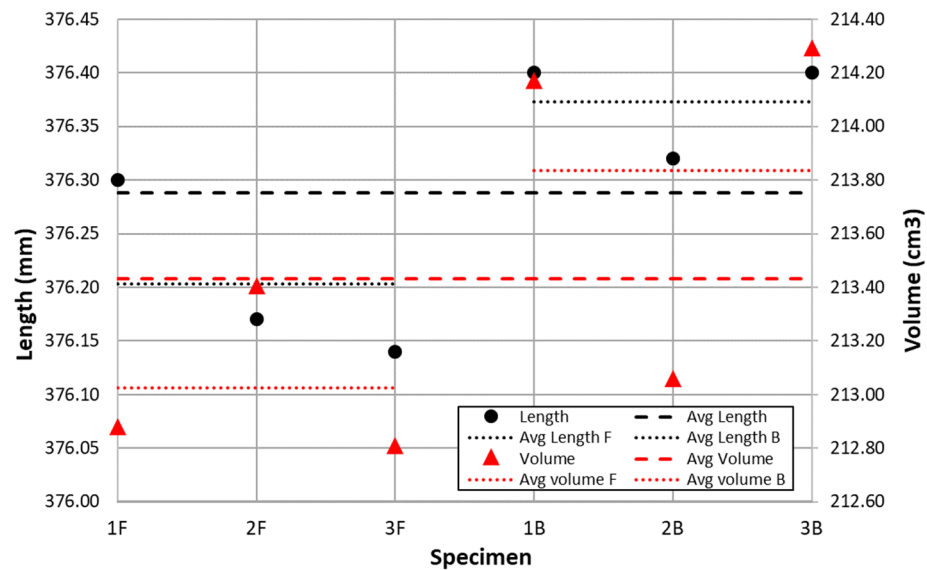


Figure 13. Plot of the six beam specimens' total length and total volume as measured from 3D scan STL files, grouped by build location. For reference, the designed nominal length (L_0) is 378.59 mm.

Despite the laser scanner not being able to completely scan all surfaces, a total volume measurement was still possible and was compared with the nominal CAD volume of 222.11 cm³. Similar to the length parameters, the largest and smallest volume specimens were 3B and 3F, respectively, where the volume of 3B measured 214.29 cm³ and that of 3F measured 212.80 cm³, giving a range of 1.49 cm³ (0.09 in³). At an assumed titanium density of 4.43 g/cc, that reveals a weight variation of 6.6 g (0.015 lbs) amongst the 6 specimens. The average volume was 213.43 cm³, which is a difference of 8.68 cm³ from the nominal, or a 3.9% reduction in volume, and the standard deviation was very small at only 0.59 cm³.

Table 1 displays the average and standard deviation of the specimens grouped by build location. Among those in the same location, the variation is smaller than the overall range. In Figure 13, the specimens were also grouped by location within the build chamber

instead of by build number, displaying the beams printed in the front of the chamber followed by those printed in the back. From this perspective, with the same part geometry, there is more significant dimensional deviation based on location within a build than from a series of builds. With respect to length, all the front specimens were shorter than those in the back, and while there was one back beam that had a volume measurement similar to the front beams, the average volume of the back beams was higher.

Table 1. Average length and volume measurements of the six topology-optimized tapered box beam specimens grouped by build location and the CAD nominal values for comparison.

Specimen Group	Length (mm)	Volume (cm ³)
Avg. Front (F)	376.20	213.03
Range Front (F)	0.16	0.60
Std. Dev. Front (F)	0.07	0.27
Avg. Back (B)	376.37	213.83
Range Back (B)	0.08	1.24
Std. Dev. Back (B)	0.04	0.55
Delta Avg. (F–B)	–0.17	–0.81
Delta Std. Dev. (F–B)	0.03	–0.29
CAD Nominal	378.59	222.11

4. Discussion

In the meso-scale step-ramp experiment, the anticipated porosity from sparsely supported melt regions was revealed in the thinnest regions of the specimens. High amounts of top-layer surface-connected porosity were observed in design thicknesses below 400 μm. This experiment revealed that the intra-layer melt topology varied with a dynamically changing hatch angle. Arcam states that their EB-PBF machine control software performs hatch optimization, such that it will rotate the scan angle to optimize scan lengths. This is tied into the current compensation function process parameter for the purpose of increasing productivity by reducing the number of scan lines [24]. It also involves merging scan lines from different regions and reordering part scans.

However, different hatch angles between components of the same geometry demonstrated a source of variability. The same model, printed at different z-heights and locations within the build chamber, will result in differing dimensional deviations if the scan path of the parts throughout the layers is not identical [7,10]. The hatching history is therefore akin to weld sequencing for a large weldment assembly. A proper weld sequence will minimize distortion of the overall assembly, whereas a change in the weld sequence will change how the weld assembly distorts. Furthermore, a randomized welding sequence will result in a chaotic dimensional deviation such that no two assemblies will be identical. That was the case for the step and ramp specimens in this experiment, which is undesirable for dimensional stability, quality, and repeatability.

From the macro-scale topology-optimized tapered box beam experiment, the most significant result was that there was more variability from part location within the build chamber than there was from build to build. As exhibited by the step-ramp specimens, this was due to each part of the build having a different hatching history. When parts with identical hatching histories are compared from build to build, the dimensional variability is reduced. However, the beams were all significantly shorter than the CAD model, such that the deviation due to thermal contraction dwarfed the level of part-to-part variation by an order of magnitude. This result indicates that the EB-PBF process is repeatable, and the beams could have more closely matched the CAD model if they had been compensated for thermal expansion at the elevated build chamber temperature [21,23].

The thermal contraction of the titanium beams can be quantified by the overall length measured from the scanned surfaces. The standard equation for linear thermal expansion is shown in Equation (1):

$$\Delta L = \alpha L_0 \Delta T \quad (1)$$

assuming a Ti-6Al-4V linear coefficient of thermal expansion (CTE) (α) to be $9.70 \mu\text{m}/\text{m}\cdot^\circ\text{C}$ up to 650°C , the predicted change in length (ΔL) at an approximate 625°C change in temperature (ΔT) is 2.30 mm over the beam span, matching the average 2.30 mm deviation from nominal. This also led to a non-trivial volume deviation of 3.9% and further stresses the need for compensating CAD models for thermal expansion prior to converting them to an STL file to be manufactured in the EB-PBF process. While only Ti-6Al-4V was utilized in this work, the demonstrated mechanisms of dimensional deviation discussed here would also be seen with other materials, to varying degrees. Improved accuracy by means of implementing the same scan path for the same geometry or by compensating the model for CTE (625°C for Ti-6Al-4V) would not impact the material properties or microstructure.

5. Conclusions

Two experiments were conducted at different length scales, meso- and macro-, to quantify the dimension accuracy of the EB-PBF process using Ti-6Al-4V and to identify the sources of variability. The meso-scale experiment used thin step and ramp specimens to capture deviation as thickness increased, while the macro-scale experiment used a topology-optimized tapered box beam to ascertain the deviation across the build chamber and multiple builds. The following conclusions were reached:

- for thin samples of the same geometry, different hatching histories reduced the dimensional accuracy, causing random deviations many times the thickness, up to 4 mm;
- for large models of the same geometry, the range of dimensional deviation across three builds was 0.26 mm;
- the average 2.3 mm deviation from the nominal geometry could have been mitigated if the tapered box beam models had been compensated for thermal expansion using a ΔT of 625°C ;
- a high degree of geometric accuracy at the assembly level was demonstrated with a modeled interface clearance of 0.1 mm.

A limitation of this work is that it was only conducted using an EB-PBF system with Ti-6Al-4V, and results would likely vary if the same experiments were performed on a LB-PBF system due to the differences in beam energy and build temperature. Furthermore, the lack of a datum scheme for the specimen models complicates the repeatability of the metrological measurements. This work is directly applicable to any metal fusion processing, which would include laser-based PBF. Future work will involve the study of changes in microstructure and microhardness with respect to thermal mass as well as the characterization of internal porosity utilizing μCT .

Author Contributions: Conceptualization, M.R. and E.B.; methodology, M.R. and E.B.; software, E.B.; validation M.R. and E.B.; formal analysis, E.B.; investigation, M.R. and E.B.; resources, M.R.; data curation, M.R. and E.B.; writing—original draft preparation, E.B.; writing—review and editing, M.R. and E.B.; visualization, E.B.; supervision, M.R.; project administration, M.R.; funding acquisition, M.R. All authors have read and agreed to the published version of the manuscript.

Funding: This work was partially accomplished using facilities funded by the Joint Center for Deployment and Research in Earth Abundant Materials (JCDREAM) in Washington State. The authors sincerely acknowledge the Boeing Pennell Professorship and the Boeing Learning Together Program for educational funding in support of this work.

Data Availability Statement: Data from these experiments may be made available upon request to the corresponding author; however, any data deemed proprietary or private cannot be transferred.

Acknowledgments: The authors would like to acknowledge Bill Kuykendall of Mechanical Engineering for his assistance on the ARCAM machine during this investigation.

Conflicts of Interest: The authors declare no conflict of interest.

References

1. Seepersad, C.C. Challenges and Opportunities in Design for Additive Manufacturing. *3D Print. Addit. Manuf.* **2014**, *1*, 10–13. [[CrossRef](#)]
2. Persenot, T.; Burr, A.; Martin, G.; Buffiere, J.-Y.; Dendievel, R.; Maire, E. Effect of build orientation on the fatigue properties of as-built Electron Beam Melted Ti-6Al-4V alloy. *Int. J. Fatigue* **2019**, *118*, 65–76. [[CrossRef](#)]
3. Riedlbauer, D.; Scharowsky, T.; Singer, R.F.; Steinmann, P.; Körner, C.; Mergheim, J. Macroscopic simulation and experimental measurement of melt pool characteristics in selective electron beam melting of Ti-6Al-4V. *Int. J. Adv. Manuf. Technol.* **2017**, *88*, 1309–1317. [[CrossRef](#)]
4. Boone, N.; Zhu, C.; Smith, C.; Todd, I.; Willmott, J. Thermal near infrared monitoring system for electron beam melting with emissivity tracking. *Addit. Manuf.* **2018**, *22*, 601–605. [[CrossRef](#)]
5. Landau, E.; Tiferet, E.; Ganor, Y.; Ganeriwala, R.; Matthews, M.; Braun, D.; Chonin, M.; Ziskind, G. Thermal characterization of the build chamber in electron beam melting. *Addit. Manuf.* **2020**, *36*, 101535. [[CrossRef](#)]
6. Wojtuszewski, R.; Banas, A.; Oliwa, M. Additive manufacturing of titanium alloys. In *Annual Forum Proceedings*; AHS International: Fairfax, VA, USA, 2018; pp. 1–18.
7. Sames, W.J.; List, F.A.; Pannala, S.; Dehoff, R.R.; Babu, S.S. The metallurgy and processing science of metal additive manufacturing. *Int. Mater. Rev.* **2016**, *61*, 315–360. [[CrossRef](#)]
8. Cordero, Z.C.; Meyer, H.M.; Nandwana, P.; Dehoff, R.R. Powder bed charging during electron-beam additive manufacturing. *Acta Mater.* **2017**, *124*, 437–445. [[CrossRef](#)]
9. Zhao, X.; Dadbakhsh, S.; Rashid, A. Contouring strategies to improve the tensile properties and quality of EBM printed Inconel 625 parts. *J. Manuf. Process.* **2021**, *62*, 418–429. [[CrossRef](#)]
10. Körner, C. Additive manufacturing of metallic components by selective electron beam melting—A review. *Int. Mater. Rev.* **2016**, *61*, 361–377. [[CrossRef](#)]
11. Townsend, A.; Senin, N.; Blunt, L.; Leach, R.K.; Taylor, J.S. Surface texture metrology for metal additive manufacturing: A review. *Precis. Eng.* **2016**, *46*, 34–47. [[CrossRef](#)]
12. Newton, L.; Senin, N.; Chatzivagiannis, E.; Smith, B.; Leach, R. Feature-based characterisation of Ti6Al4V electron beam powder bed fusion surfaces fabricated at different surface orientations. *Addit. Manuf.* **2020**, *35*, 101273. [[CrossRef](#)]
13. Lee, S.; Rasoolian, B.; Silva, D.F.; Pegues, J.W.; Shamsaei, N. Surface roughness parameter and modeling for fatigue behavior of additive manufactured parts: A non-destructive data-driven approach. *Addit. Manuf.* **2021**, *46*, 102094. [[CrossRef](#)]
14. Flys, O.; Berglund, J.; Rosén, B.-G. Using confocal fusion for measurement of metal AM surface texture. *Surf. Topogr. Metrol. Prop.* **2020**, *8*, 024003. [[CrossRef](#)]
15. Lou, S.; Zhu, Z.; Zeng, W.; Majewski, C.; Scott, P.J.; Jiang, X. Material ratio curve of 3D surface topography of additively manufactured parts: An attempt to characterise open surface pores. *Surf. Topogr. Metrol. Prop.* **2021**, *9*, 015029. [[CrossRef](#)]
16. Thompson, A.; Senin, N.; Giusca, C.; Leach, R. Topography of selectively laser melted surfaces: A comparison of different measurement methods. *CIRP Ann. Manuf. Technol.* **2017**, *66*, 543–546. [[CrossRef](#)]
17. Wang, P.; Sin, W.J.; Nai, M.L.S.; Wei, J. Effects of Processing Parameters on Surface Roughness of Additive Manufactured Ti-6Al-4V via Electron Beam Melting. *Materials* **2017**, *10*, 1121. [[CrossRef](#)] [[PubMed](#)]
18. Seewig, J.; Scott, P.J.; Eifler, M.; Barwick, B.; Hüser, D. Crossing-The-Line Segmentation as a Basis for Rsm and Rc Evaluation. *Surf. Topogr. Metrol. Prop.* **2020**, *8*, 024010. [[CrossRef](#)]
19. Bukkapatnam, S.T.; Iquebal, A.S.; Kumara, S.R. Planar random graph representations of spatiotemporal surface morphology: Application to finishing of 3-D printed components. *CIRP Ann.* **2018**, *67*, 495–498. [[CrossRef](#)]
20. Du Plessis, A.; Tshibalanganda, M.; Yadroitsava, I.; Yadroitsev, I. On the Evaluation of Surface Roughness: X-ray Tomography Reveals Hidden Details. In *Progress in Additive Manufacturing 2020*; Shamsaei, N., Seifi, M., Eds.; ASTM International: West Conshohocken, PA, USA, 2022; pp. 208–222.
21. Gao, W.; Zhang, Y.; Ramanujan, D.; Ramani, K.; Chen, Y.; Williams, C.B.; Wang, C.C.L.; Shin, Y.C.; Zhang, S.; Zavattieri, P.D. The status, challenges, and future of additive manufacturing in engineering. *Comput.-Aided Des.* **2015**, *69*, 65–89. [[CrossRef](#)]
22. Marrugo, A.G.; Gao, F.; Zhang, S. State-of-the-art active optical techniques for three-dimensional surface metrology: A review. *J. Opt. Soc. Am. A* **2020**, *37*, B60. [[CrossRef](#)]
23. Leach, R.; Bourell, D.; Carmignato, S.; Donmez, A.; Senin, N.; Dewulf, W. Geometrical metrology for metal additive manufacturing. *CIRP Ann.* **2019**, *68*, 677–700. [[CrossRef](#)]
24. Smith, C.; Derguti, F.; Nava, E.H.; Thomas, M.; Tammam-Williams, S.; Gulizia, S.; Fraser, D.; Todd, I. Dimensional accuracy of Electron Beam Melting (EBM) additive manufacture with regard to weight optimized truss structures. *J. Mater. Process. Technol.* **2016**, *229*, 128–138. [[CrossRef](#)]
25. Ameta, G.; Fox, J.; Witherell, P. Tolerancing and Verification of Additive Manufactured Lattice with Supplemental Surfaces. *Procedia CIRP* **2018**, *75*, 69–74. [[CrossRef](#)]

26. Gruber, S.; Grunert, C.; Riede, M.; López, E.; Marquardt, A.; Brueckner, F.; Leyens, C. Comparison of dimensional accuracy and tolerances of powder bed based and nozzle based additive manufacturing processes. *J. Laser Appl.* **2020**, *32*, 032016. [[CrossRef](#)]
27. Bol, E.; Doyle, C.; Ramulu, M. Process Parameter Effects on Melt Topology and Dimensional Deviation in Electron Beam Melted Ti-6Al-4V. In Proceedings of the ASME 2021 International Mechanical Engineering Congress and Exposition, Virtual, 1–5 November 2021; American Society of Mechanical Engineers: New York, NY, USA, 2021; Volume 85550, p. V02AT02A011.
28. Bol, E.; Ramulu, M. Repeatability of a Topology Optimized Tapered Box Beam Additively Manufactured with Electron Beam Melted Ti-6Al-4V. In Proceedings of the ASME 2020 International Mechanical Engineering Congress and Exposition, Virtual, 16–19 November 2020; American Society of Mechanical Engineers: New York, NY, USA, 2020; Volume 84485, p. V02AT02A049.
29. Zhang, X.; Leary, M.; Tang, H.; Song, T.; Qian, M. Selective electron beam manufactured Ti-6Al-4V lattice structures for orthopedic implant applications: Current status and outstanding challenges. *Curr. Opin. Solid State Mater. Sci.* **2018**, *22*, 75–99. [[CrossRef](#)]
30. Damri, E.; Tiferet, E.; Braun, D.; Ganor, Y.; Chonin, M.; Orion, I. Effects of Gas Pressure during Electron Beam Energy Deposition in the EBM Additive Manufacturing Process. *Metals* **2021**, *11*, 601. [[CrossRef](#)]
31. Bendsøe, M.P. Optimal shape design as a material distribution problem. *Struct. Optim.* **1989**, *1*, 193. [[CrossRef](#)]
32. Zhou, M.; Rozvany, G. The COC algorithm, Part II: Topological, geometrical and generalized shape optimization. *Comput. Methods Appl. Mech. Eng.* **1991**, *89*, 309–336. [[CrossRef](#)]
33. Mlejnek, H.P. Some aspects of the genesis of structures. *Struct. Optim.* **1992**, *5*, 64–69. [[CrossRef](#)]
34. Muñoz, D.; Nadal, E.; Albelda, J.; Chinesta, F.; Ródenas, J. Allying topology and shape optimization through machine learning algorithms. *Finite Elem. Anal. Des.* **2022**, *204*, 103719. [[CrossRef](#)]
35. Zhang, L.-C.; Wang, J.; Liu, Y.; Jia, Z.; Liang, S.-X. Additive manufacturing of titanium alloys. In *Reference Module in Materials Science and Materials Engineering*; Elsevier: Amsterdam, The Netherlands, 2020.

Disclaimer/Publisher’s Note: The statements, opinions and data contained in all publications are solely those of the individual author(s) and contributor(s) and not of MDPI and/or the editor(s). MDPI and/or the editor(s) disclaim responsibility for any injury to people or property resulting from any ideas, methods, instructions or products referred to in the content.